



Publication Year	2017
Acceptance in OA @INAF	2020-12-30T13:14:25Z
Title	Can Sgr A* flares reveal the molecular gas density PDF?
Authors	Churazov, E.; Khabibullin, I.; Sunyaev, R.; PONTI, GABRIELE
DOI	10.1093/mnras/stx1855
Handle	http://hdl.handle.net/20.500.12386/29374
Journal	MONTHLY NOTICES OF THE ROYAL ASTRONOMICAL SOCIETY
Number	471

Can Sgr A* flares reveal the molecular gas density PDF?

E. Churazov,^{1,2★} I. Khabibullin,^{1,2} R. Sunyaev^{1,2} and G. Ponti³

¹*MPI für Astrophysik, Karl-Schwarzschild str. 1, Garching D-85741, Germany*

²*Space Research Institute, Profsoyuznaya str. 84/32, Moscow 117997, Russia*

³*MPI für extraterrestrische Physik, Giessenbachstrasse 1, Garching D-85748, Germany*

Accepted 2017 July 18. Received 2017 July 18; in original form 2017 May 16

ABSTRACT

Illumination of dense gas in the Central Molecular Zone by powerful X-ray flares from Sgr A* leads to prominent structures in the reflected emission that can be observed long after the end of the flare. By studying this emission, we learn about past activity of the supermassive black hole in our Galactic Center and, at the same time, we obtain unique information on the structure of molecular clouds that is essentially impossible to get by other means. Here we discuss how X-ray data can improve our knowledge of both sides of the problem. Existing data already provide (i) an estimate of the flare age, (ii) a model-independent lower limit on the luminosity of Sgr A* during the flare and (iii) an estimate of the total emitted energy during Sgr A* flare. On the molecular clouds side, the data clearly show a voids-and-walls structure of the clouds and can provide an almost unbiased probe of the mass/density distribution of the molecular gas with the hydrogen column densities lower than few 10^{23} cm^{-2} . For instance, the probability distribution function of the gas density PDF(ρ) can be measured this way. Future high energy resolution X-ray missions will provide the information on the gas velocities, allowing, for example, a reconstruction of the velocity field structure functions and cross-matching the X-ray and molecular data based on positions and velocities.

Key words: radiative transfer – ISM: clouds – Galaxy: centre – galaxies: nuclei – X-rays: general – X-rays: individual: Sgr A*.

1 INTRODUCTION

While the supermassive black hole Sgr A* at the centre of the Milky Way is currently very dim (e.g. Baganoff et al. 2003), it has experienced powerful flares of X-ray radiation in the recent past. The historical records of these flares are revealed by reflected/reprocessed radiation coming from dense molecular clouds (Sunyaev, Markevitch & Pavlinsky 1993; Koyama et al. 1996). The imprints left by the flares in spatial and time variations of the reflected emission suggest that a powerful flare happened some hundred years ago (see e.g. Ponti et al. 2013, for review). It lasted less than several years (e.g. Clavel et al. 2013; Churazov et al. 2017a) and Sgr A* was more than million times brighter than today. The energetics of the flare can be provided by a relatively modest tidal disruption event (e.g. Zubovas, Nayakshin & Markoff 2012; Guillochon et al. 2014), although many issues remain unresolved.

Clearly, molecular clouds offer us a convenient tool to study Sgr A*'s past history. At the same time, the flare itself serves as an extremely powerful probe of molecular gas. We, in particular, argue that the X-ray illumination opens a new way of measuring the properties of the gas density and velocity distributions in

molecular clouds. The probability distribution function¹ of the gas density PDF(ρ) inside a molecular cloud is shaped by a complex interplay between supersonic turbulence, self-gravity, magnetic fields and stellar feedback – the key agents in the current ISM paradigm (see e.g. Elmegreen & Scalo 2004; Mac Low & Klessen 2004; McKee & Ostriker 2007; Klessen & Glover 2016, for reviews). As a result, it bears invaluable information on how this interplay actually proceeds and in which way it determines the dynamical state of the cloud (e.g. Federrath et al. 2010). The PDF(ρ) is believed to be intimately connected to the stellar initial mass function and the efficiency of star formation (e.g. Padoan & Nordlund 2002; Mac Low & Klessen 2004). Molecular clouds in the Central Molecular Zone (CMZ) are of particular interest in this context, since they evolve in a very specific environment of the Galactic Center, and also because their measured star formation efficiency appears to be an order of magnitude lower compared to the molecular clouds in the Galactic disc (Longmore et al. 2013; Kruijssen et al. 2014; Ginsburg et al. 2016; Kauffmann et al. 2017a; Barnes et al. 2017). Measuring the PDF(ρ) over a broad range of the scales is a key for clarifying the particular mechanism(s) responsible for the suppression

¹ Throughout the paper we use ‘Probability Distribution Function’ in place of a more common ‘Probability Density Function’ to avoid confusion with gas density.

* E-mail: churazov@mpa-garching.mpg.de

Table 1. Road map for probing Sgr A* flare and molecular clouds with X-ray data.

Parameter	Methods & [Instruments]	Section
t_{age}	Structure functions in time and space [<i>Chandra</i> , <i>XMM-Newton</i> (multiple observations)] Equivalent width of the 6.4 keV line [<i>Chandra</i> , <i>XMM-Newton</i>] Polarization [future X-ray polarimetric missions, e.g. <i>XIPE</i> or <i>IXPE</i>]	Section 2.1
Δt	Structure functions in time and space [<i>Chandra</i> , <i>XMM-Newton</i> (multiple observations)] Smallest clouds [<i>Chandra</i> (deep + multiple observations)]	Section 2.2
$L_{X, \text{min}}$	Brightest clouds [<i>Chandra</i> (deep)]	Section 2.3.2
$L_X(t)$	Smallest clouds [<i>Chandra</i> (deep + multiple observations)]	Section 2.2
$L_X \Delta t$	X-ray images + molecular data [<i>Chandra</i> , <i>XMM-Newton</i>]	Section 2.3.2
$dV/d\rho$	Deep X-ray image [<i>Chandra</i> (deep)]	Section 3
$\rho(l, b, z)$	X-ray images [<i>Chandra</i> , <i>XMM-Newton</i> (multiple observations)]	Section 3
$v_z(l, b, z)$	High-resolution X-ray spectroscopy (Athena, Lynx)	Section 3.3
$v(l, b, z)$	Proper motions from masers	Section 3.3

of star formation, e.g. high level of solenoidally forced turbulence (Federrath et al. 2016), and also whether this is a generic property of such an environment or it differs from a cloud to cloud, e.g. as a result of the different orbital evolution histories (Kauffmann et al. 2017b). Similarly important is the information on the properties of the velocity field (e.g. Boldyrev 2002; Kritsuk et al. 2007), which can be characterized, e.g. by its structure function. Unfortunately, direct measurement of the PDF(ρ) or the velocity structure function based on molecular emission lines is hindered by the projection effects, although various (model-dependent) de-projection techniques have been proposed and tested on the data (e.g. Stutzki et al. 1998; Brunt, Federrath & Price 2010; Kainulainen, Federrath & Henning 2014). Further complication comes from the fact that the commonly used gas tracers are sensitive to a certain range of densities determined by self-absorption and collisional de-excitation (Genzel 1991). Below we argue that this limitation for the density distribution can be lifted by using X-ray observations of clouds illuminated by the Sgr A* flare. This can be done with the current generation of X-ray observatories. Future X-ray observatories, including cryogenic bolometers and polarimeters, will further boost our ability to conduct in-depth studies of molecular gas, providing, in particular, a possibility to measure the structure function of the velocity field (almost) free from the projection effects.

In the previous two papers, Churazov et al. (2017a and 2017b, hereafter C17a and C17b) we have considered constraints on the age of the flare, reconstruction of the 3D distribution of molecular gas and the expected long-term evolution of the reflected emission. Here we focus more on the internal structure of molecular clouds and also outline a roadmap for detailed diagnostics of the molecular gas using current and future observatories. In lieu of the description of the paper structure, we refer to Table 1, which provides a summary of possible measurements and links to the relevant sections. In this paper we consider only the molecular clouds in the so-called ‘Bridge’ and G0.11-0.11, as these clouds are currently the brightest in the reflected emission.

2 PARAMETERS OF THE SGR A* FLARE

The reflected emission is formed as a result of interplay between three processes: Compton scattering, photoelectric absorption and fluorescence. For the energy band of interest here ($\sim 4\text{--}8$ keV), there is no big difference between scattering by free electrons or electrons bound in hydrogen atoms or molecules unless the spectral resolution is high enough to resolve fine structure of the fluorescent lines caused by multiple scatterings (Sunyaev & Churazov 1996;

Vainshtein, Syunyaev & Churazov 1998; Sunyaev, Uskov & Churazov 1999). *Chandra* images of the reflected emission from 7×9 arcmin region centred at $(l, b) \sim (0.1, -0.08)$ taken in 2000, 2013 and 2015 are shown in Fig. 1 (see C17a for the details on the generation of reflected emission maps). In short, the observed spectra in each pixel of an image are decomposed into a linear combination of two components: one has a characteristic reflected spectrum with neutral iron 6.4 keV line and another having a spectrum of ~ 6 keV optically thin plasma, to account for contribution of old stellar population. The normalizations of each component form two images. From these images it is clear that the reflected emission is highly structured and it varies strongly on scales of 10 years or shorter. In addition, direct spectral measurements of the variable emission show that its spectral shape is consistent with the reflection scenario (see fig. 4 in C17b).

The data on the reflected emission from molecular clouds provide us several ways to probe the X-ray light curve $L_X(t)$ of Sgr A* flare. As the first step one can adopt a simplified model of the flare, by parameterizing it with three parameters – the age of the flare t_{age} , its duration Δt and luminosity L_X . Of course, there are other parameters affecting the problem, e.g. the shape of the flare spectrum, abundance of heavy elements in the gas, etc., which are to be taken into account in the detailed quantitative model. In this section we first discuss the constraints that can be placed on t_{age} , Δt , L_X and assume that the flare emission is isotropic.

2.1 Age of the flare

The age of the flare t_{age} (the time elapsed since the onset or end of the flare till the time of observation) is an important parameter that is tightly linked to the position of the reflected cloud with respect to Sgr A*. Indeed, the time delay arguments (Couderc 1939; Sunyaev & Churazov 1998) imply that

$$z = \frac{c}{2} t_{\text{age}} - \frac{R^2}{2c t_{\text{age}}}, \quad (1)$$

where z and R are the line-of-sight and projected distances of the cloud from Sgr A*, respectively; c is the speed of light. Since R is directly measured, for a short flare there is a one-to-one correspondence between z and t_{age} . This is further illustrated in Fig. 2, which schematically shows the locus of the illuminated gas for a short flare.

There are several possibilities to measure z or t_{age} , which we discuss below.

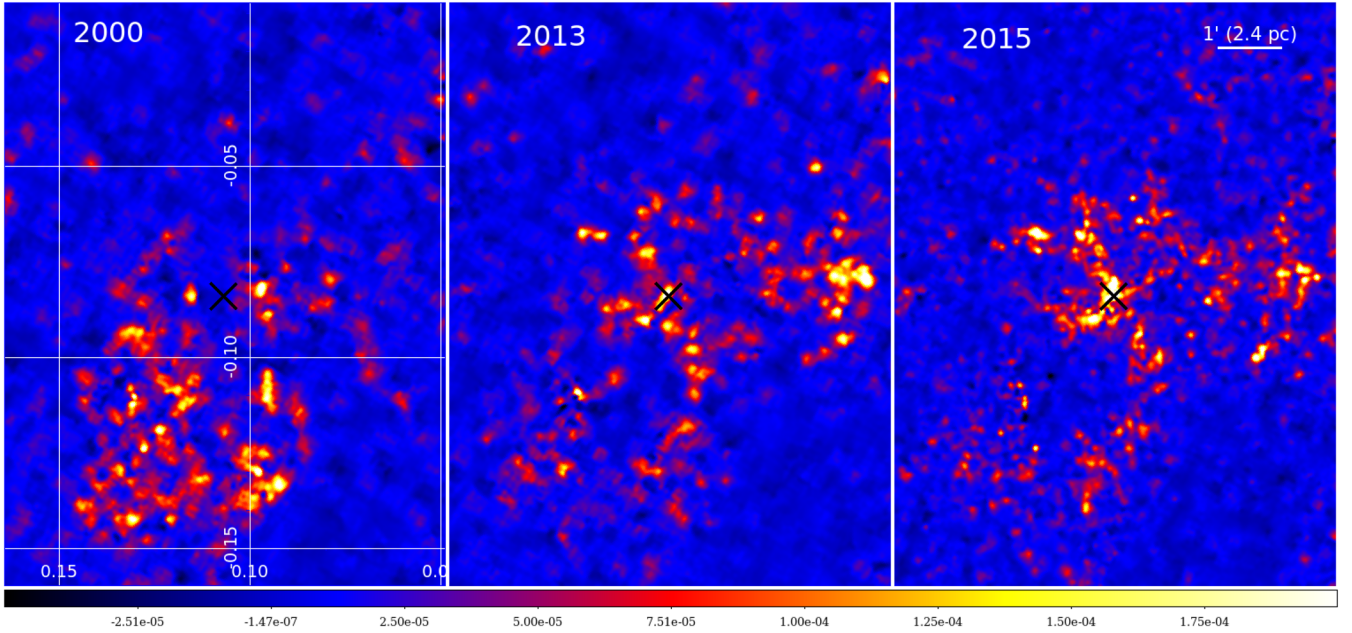


Figure 1. *Chandra* images of the reflected emission in a 7×9 arcmin region centred at $(l, b) \sim (0.1, -0.08)$ in 2000, 2013 and 2015. The images have been adaptively smoothed to get the same number of raw counts in the 4–8 keV band under a boxcar smoothing window. Images are shown in galactic coordinates. In a ‘short-flare’ scenario, these images provide us a view of thin slices of gas ($\Delta z \sim 0.2\Delta t_{\text{yr}}$ pc, where Δt_{yr} is the duration of the flare in years) through different layers of the gas. For observations separated by more than the duration of the flare, i.e. by several years, these slices do not overlap. The 2013 and 2015 images show a clear ‘voids and walls’ structure of the molecular complex, resembling a typical outcome of numerical models (see e.g. fig. 9 in Clark et al. 2012). The earlier 2000 image gives an impression that the slice (in the bottom-left part of the image) is going through one of the ‘walls’ of the molecular complex. Such slices are direct probes of the 3D density structure of this molecular complex. Black cross in all three images marks the brightest region in 2015 image.

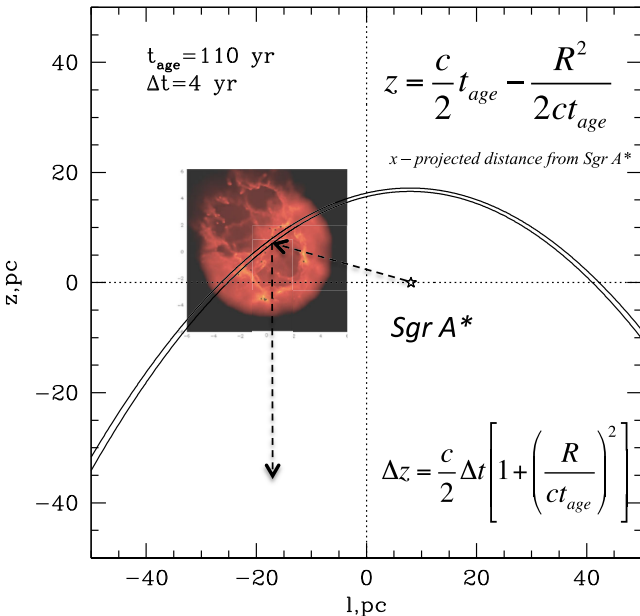


Figure 2. Sketch of a molecular cloud exposed to a 4-yr-long flare that happened 110 years ago (a view on the Galactic Center region from above the Galactic Plane). An image of a simulated cloud (from Walch et al. 2012) is used for illustration. Star marks the position of Sgr A*. The light propagates from Sgr A* to the cloud and then to the observer. The locus of illuminated gas is a space between two parabolas (see equation (1)). Only this gas should be visible in X-ray images. The thickness Δz of the illuminated region along the line of sight is related to the duration of the flare Δt and the projected distance x from Sgr A*. The value $\Delta t = 4$ yr is used only for illustration.

2.1.1 Comparison of time and space domains

As discussed in C17a, the assumption that a small-scale substructure of molecular clouds is isotropic in space allows one to determine the age of the flare by comparing the structure functions of reflected emission in time and space domains. If the flare is short, then even from a single image, like one of those shown in Fig. 1, we have detailed information on the space structure function of the illuminated gas (see Section 3.2 below). By observing the same region many times, we get information on the time domain structure function. But for a short flare this time domain structure function is essentially the space domain structure function, subject to a simple transformation due to the velocity of the flare propagation along the line of sight $v_z = \frac{\partial z}{\partial t}$. This value defines the shift $v_z \delta t$ of the illuminated region along the line of sight between observations separated by a given time δt . Comparing space and time domain functions, one can find v_z , which turns out to be $\sim 0.7c$ (C17a). The value of v_z depends on the age of the flare

$$v_z = \frac{c}{2} \left[1 + \left(\frac{R}{ct_{\text{age}}} \right)^2 \right]. \quad (2)$$

Therefore, knowing v_z one can determine the age of the flare $t_{\text{age}} \sim 110$ yr. While the accuracy of this approach is limited by the amount of available data and rests on the assumption that on small scales the clouds are isotropic, the accuracy may improve in future, when more data become available.

A more subtle diagnostics is possible from the elongation of illuminated clouds perpendicular to the direction towards Sgr A* (see Sunyaev & Churazov 1998 and C17a), since the locus of illuminated region makes an angle to the line of sight, and this angle depends on the location of the cloud and t_{age} . This should lead to the difference

in structure functions calculated along radial (towards Sgr A*) and tangential directions.

2.1.2 Spectral analysis

Another possibility to determine z is to use the dependence of the equivalent width of the iron line in the reflected emission on the scattering angle (Sunyaev & Churazov 1998). Since the fluorescent line is emitted isotropically, while the scattered continuum intensity $\propto(1 + \mu^2)$, the equivalent width varies by a factor of 2 when the scattering angle changes from 0 to 90 deg. Therefore, fitting the spectra, one can infer the scattering angle. Such approach has been used in, e.g. Capelli et al. (2012); Walls et al. (2016); Krivonos et al. (2017). The accuracy of this approach is somewhat limited by the uncertainties in the heavy elements abundance and the quality of modelling of other background/foreground components. The latter limitation can be lifted by, e.g. considering the regions where reflected component dominates the spectrum, simultaneously fitting the spectra during and before/after the flare (Clavel et al. 2013), or fitting only the variable part of the emission (C17b).

2.1.3 Future polarization data

A straightforward way of determining z (and, therefore, t_{age}) is possible with future X-ray polarization measurements (Churazov, Sunyaev & Sazonov 2002; Marin et al. 2015; Molaro, Khatri & Sunyaev 2016, C17b). Effectively, the degree of polarization P is a proxy of the scattering angle θ . More precisely, $P \approx (1 - \mu^2)/(1 + \mu^2)$, where $\mu = \cos \theta$. The uncertainty in the sign of θ can likely be resolved based on the spectral data and the light curve. Once θ is known, the value of z can immediately be derived from the projected distance R of the cloud from Sgr A*. Knowing R and z , the age of the flare can be determined from equation (1). The sensitivity of future X-ray polarimeters like *XIPE* and *IXPE* (Soffitta et al. 2013; Weisskopf et al. 2013) should be sufficient to measure the degree of polarization and, therefore, t_{age} . More importantly, a comparison of the polarization degree from different clouds is a powerful test of the single-flare scenario that for a given t_{age} makes definite prediction of P as a function of projected distance from Sgr A*. Furthermore, the direction of the polarization plane, which should be perpendicular to the direction to the primary source, is probably the most robust way to verify that for all clouds the source position is consistent with the location of Sgr A*, in contrast with the assumption that individual clouds are illuminated by less luminous flares of stellar-mass X-ray objects local to these clouds (see e.g. a discussion of the reflected emission from the black hole binary 1E1740.7-2942 embedded in the cloud in Sunyaev et al. 1991; Churazov et al. 1993).

2.2 Duration of the flare

Duration of the flare Δt is one of the important parameters that can be derived from observation. Below we briefly discuss two ways of determining Δt . We assume below that there was only one recent flare, unless explicitly stated otherwise.

2.2.1 Light curves from individual clouds

The simplest and most direct way of constraining Δt is by studying the variability of a (small) molecular cloud in reflected emission. Let us consider reflected emission coming from one particular direction. Any given atom/electron is producing reflected emission over time

interval Δt (if we neglect multiple scatterings). A molecular cloud, occupying a large region along the line of sight, will remain bright longer than Δt , because various parts of the cloud are illuminated at different times. The time-scale of the illumination front propagation through the cloud is $\Delta t_c \sim l_z/v_z$, where l_z is the characteristic size of the cloud along the line of sight² and v_z depends on the position of the cloud and the age of the flare t_{age} (see Section 2.1). For example, in C17a we estimated $v_z \sim 0.7c$ for the Bridge complex. From these arguments it is clear that (i) the shortest observed flare places a conservative limit on Δt and (ii) systematic search of short flares for the smallest clouds is the best strategy to provide the tightest constraints on the duration of the flare. Moreover, if the cloud is small (i.e. $\Delta t_c \ll \Delta t$) and relatively isolated, then the observed light curve from such cloud would be a direct probe of the Sgr A* light curve $L_X(t)$.

The variability of reflected emission has been modelled in many studies (e.g. Sunyaev & Churazov 1998; Clavel et al. 2014, C17b). Observationally, it was first reported in Munro et al. (2007) and then found in all regions bright in the reflected emission (e.g. Ponti et al. 2010; Terrier et al. 2010; Capelli et al. 2012; Clavel et al. 2013; Ryu et al. 2013; Mori et al. 2015; Zhang et al. 2015). By now it is clear that Sgr A* was variable on time-scales as short as several years (and, perhaps, on even shorter time-scales). More constraints will come soon from the multiple ~ 100 ks observations of the Bridge region with *Chandra* (PI: Maica Clavel). An ultimate set of constraints on the duration could come from a set of very deep *Chandra* observations that can probe the smallest clouds (see Section 3).

2.2.2 Comparison of time and space domains

Yet another possibility to determine Δt was outlined in C17a. Instead of studying individual clouds, one can compare statistical properties of the reflected emission in space and time domains. Basically, one calculates a correlation (or structure) function for the reflected signal as a function of separation in space and time and then compares these functions. As long as the substructure in the gas density distribution is isotropic, one identify the effect of an extended flare (finite Δt) via its impact on to the time domain correlation function. So far we did not see clear signatures of finite duration (see C17a), but the data from ongoing *Chandra* observations will likely have much better diagnostic power than the existing data sets.

The advantage of this approach is that all data are used to place constraints on Δt (rather than a light curve for a single cloud). The approach, however, requires an assumption that there is no difference in the statistics of small-scale structures along and perpendicular to the line of sight. Also, to get unbiased results from the comparison of structure functions, one has to take into account variations of the telescope angular resolution across the studied field, unless the images are heavily binned.

2.3 Luminosity and total emitted energy

2.3.1 Lower limit on the luminosity of Sgr A*

Consider a uniform cloud of neutral gas, illuminated by a parallel beam of X-ray emission with a power-law spectrum with photon

² If we do not resolve the cloud, then one has to consider propagation time-scales for all directions, which depend on the geometry of the cloud and its orientation with respect to the propagating front. The longest time-scale will set the lifetime of the observed reflected emission caused by an infinitely short flare of the primary source.

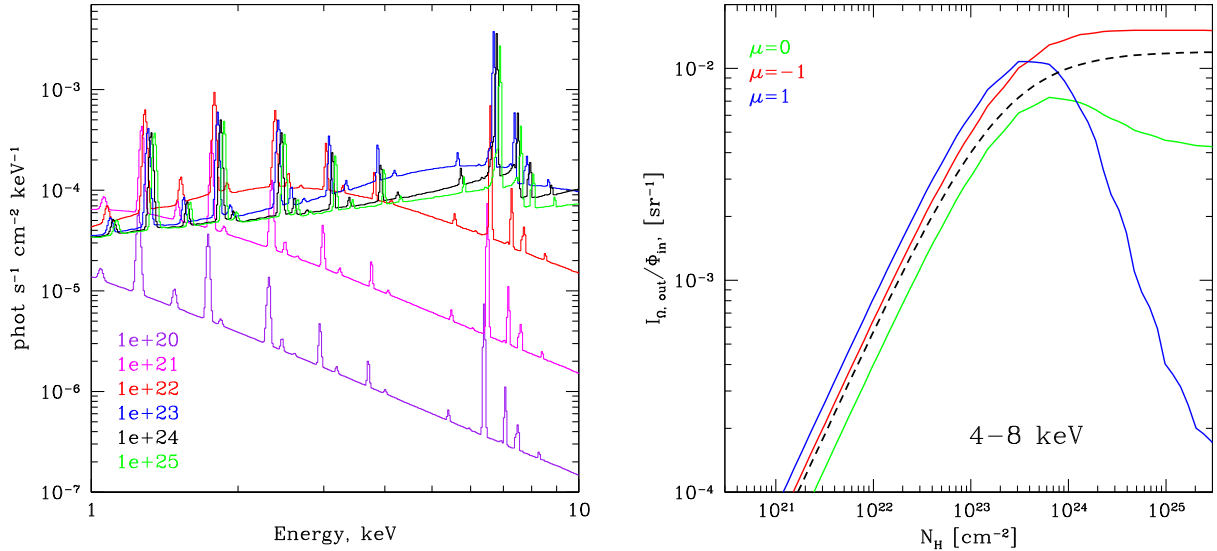


Figure 3. Dependence of the reflected intensity on the column density and the scattering angle. Left: Reflected spectra for a uniform spherical cloud of neutral gas illuminated by a parallel beam of X-rays with the power-law spectrum with photon index $\Gamma = 1.9$ for different values of the column densities N_{H} along the diameter of the cloud. The scattering angle is 90 deg. The `CREFL16` model (C17b) was used to generate the spectra. For small-column densities the scattered continuum follows the shape of the incident spectrum and scales linearly with N_{H} . At large column densities the spectrum shape and normalization become independent on N_{H} . Right: The ratio of radiant intensity to the incident flux in the 4–8 keV band as a function of N_{H} for three scattering angles: 90 deg ($\mu = 0$, green), 0 deg ($\mu = 1$, blue) and 180 deg ($\mu = -1$, red). The dashed line is a crude approximation of this ratio (see equation (3) in the text).

index $\Gamma = 2$. Typical emergent spectra are shown in Fig. 3 (left-hand panel) for the scattering angle $\theta = 90$ deg ($\mu = 0$). In all cases the impinging energy flux Φ_{in} is the same, but the column density of the cloud varies from 10^{20} to 10^{25} cm $^{-2}$. From Fig. 3 it is clear that when the column density is large, the efficiency of scattering becomes independent on N_{H} . This happens at $N_{\text{H}} \sim 3 \cdot 10^{23}$ cm $^{-2}$, the value that incidentally is not far from typical column densities for molecular clouds in the CMZ (e.g. Mills & Battersby 2017). For much larger column densities, the deepest layers of the cloud are completely screened from the illuminating radiation and do not contribute to the scattering signal.

We can characterize the efficiency of reflection by the quantity

$$\eta(N_{\text{H}}) = \frac{I_{\Omega, \text{out}}}{\Phi_{\text{in}}} \text{sr}^{-1} \quad (3)$$

where $I_{\Omega, \text{out}}$ is the intensity of reflected emission in a given direction (per unit solid angle), while Φ_{in} is the total energy flux of X-ray radiation entering the cloud per unit time. The dependence of η on N_{H} and μ is shown in the right-hand panel of Fig. 3. The dashed line in Fig. 3 (left-hand panel) shows the following crude approximation

$$\eta(N_{\text{H}}) \approx 1.2 \cdot 10^{-2} \frac{N_{\text{H}, 23}}{2 + N_{\text{H}, 23}} \lesssim 1.2 \cdot 10^{-2}, \quad (4)$$

where $N_{\text{H}, 23}$ is the column density in units 10^{23} cm $^{-2}$. Thus, for small column densities $\eta(N_{\text{H}}) \lesssim 6 \cdot 10^{-3} N_{\text{H}, 23}$, while for very large column densities $\eta(N_{\text{H}}) \lesssim 1.2 \cdot 10^{-2}$. The very fact that $\eta(N_{\text{H}})$ does not exceed certain value implies that one can use the maximal observed surface brightness of the reflected emission to obtain a lower limit on the luminosity of the illuminating source. To do this, we have selected a small circular region with the radius of 2.8 arcsec centred at the brightest spot in the 2015 images (see the black X in Fig. 1). The spectrum extracted from this region has strong fluorescent line at 6.4 keV and can be described as an almost pure reflection component. Using the absorption-corrected 4–8 keV surface brightness in the 4–8 keV band ($I_{\text{X}} \sim 6 \cdot 10^{-12}$ erg s $^{-1}$ cm $^{-2}$ arcmin $^{-2}$) and the maximal value of $\eta(N_{\text{H}}) \sim 10^{-2}$ we have estimated the incident

flux Φ_{in} in the same energy band. Finally, the luminosity of Sgr A* was estimated by calculating the solid angle of the cloud as seen from the Sgr A* position, $L_{\text{X}, 4-8 \text{ keV}} = \Phi_{\text{in}} 4\pi D_{\text{sc}}^2 \sim 6 \cdot 10^{38}$ erg s $^{-1}$, where $D_{\text{sc}} \approx 26$ pc is the assumed distance from Sgr A* to the cloud (C17a). Recalculating 4–8 keV luminosity to other energy bands assuming photon index of 2.0, we obtain the final result: the lower limit on the luminosity $L_{\text{X}, \text{min}}$ of Sgr A*, needed to generate observed surface brightness is $\sim 10^{39}$ and $\sim 4 \cdot 10^{39}$ erg s $^{-1}$ in the 2–10 and 1–100 keV bands, respectively. Such level of luminosity could in principle be provided by a stellar mass binary in the vicinity of the Galactic Center, rather than by Sgr A* itself.

Note that this is a conservative estimate, given that the conditions required for maximal reflection efficiency may not be satisfied in the studied region. To reach the maximum efficiency, the cloud has to be illuminated from the side facing the observer and the optical depth of the illuminated region along the line of sight has to be larger than $\sim 3 \cdot 10^{23}$ cm $^{-2}$.

Of course, other parameters, like the scattering angle, abundance of heavy elements, etc., also affect the estimates of L_{X} . Variations in these parameters lead to changes in the luminosity estimate by factors of order 2, unless we consider extreme values of the parameters.

2.3.2 Total energy emitted by Sgr A* during the flare

Observations suggest that the reflected X-ray flux varies on scales as small as few years (e.g. Clavel et al. 2013). In our minimalistic model we assume that there was only one flare over the last several hundred years. If so, the size of the illuminated slice along the line of sight is $v_z \Delta t \sim 0.2 \Delta t_{\text{yr}}$ pc, where Δt_{yr} is the duration of the flare in years (see fiducial parameters in Section 2.1). This value is much smaller than the characteristic size of prominent molecular complexes, like, e.g. Bridge that has a diameter of ~ 10 pc. Therefore, the flare illuminates only a thin slice of the molecular complex. The mean density of this slice can be estimated, assuming that it is the same as the mean density of the entire complex.

To this end, we used the total H_2 mass of the GCM0.11-0.08 cloud $M \sim 1.3 \cdot 10^5 M_\odot$ from Mills & Battersby (2017) based on the integrated line intensities in HCN and N_2H^+ (see their Fig. 3). This mass corresponds to a rectangular region 5×2 arcmin (or 12×5 pc). We assume that the size of the molecular complex along the line of sight is a geometric mean between the length and the width of the region, i.e. $\sqrt{2 \times 5} = 3.2$ arcmin. The derived mean density (from the mass and volume of the region) is $\bar{\rho}_H \sim 10^4 \text{ cm}^{-3}$. Thus, the mean column density of the illuminated layer $N_H \sim \bar{\rho}_H v_z \Delta t \sim 7 \times 10^{21} \text{ cm}^{-2}$. Therefore, the Thompson depth of the layer is small and the reflected flux scales linearly with the illuminating flux and the mass of the illuminated gas (see Fig. 3). Thus, the observed surface brightness of the reflected emission is

$$I_X = \frac{L_X}{4\pi D_{sc}^2} \bar{\rho}_H v_z \Delta t \frac{\sigma_{4-8}}{4\pi}, \quad (5)$$

where σ_{4-8} is the effective scattering cross-section in the 4–8 keV band. For an optically thin medium, σ_{4-8} can be evaluated from the value $\eta(N_H)$ by rewriting equation (3) for the limit of $N_H \rightarrow 0$ as the ratio of the scattered flux to the illuminating flux entering a cloud with radius r_c

$$\eta(N_H) = \frac{\frac{4}{3}\pi r_c^3 \bar{\rho}_H \frac{\sigma_{4-8}}{4\pi} \frac{L_X}{4\pi D_{sc}^2}}{\pi r_c^2 \frac{L_X}{4\pi D_{sc}^2}} = \frac{r_c \bar{\rho}_H}{3\pi} \sigma_{4-8} = \frac{N_H}{6\pi} \sigma_{4-8}, \quad (6)$$

where $N_H = 2r_c \bar{\rho}_H$ is the hydrogen column density of the cloud. The approximation given by equation (4) (see the dashed line in Fig. 3) implies

$$\sigma_{4-8} \sim \frac{6\pi \eta(N_H)}{N_H} \sim 1.1 \cdot 10^{-24} \text{ cm}^2 \approx 1.7 \sigma_T. \quad (7)$$

It is larger than the Thomson cross-section per hydrogen atom due to (i) the presence of electrons in helium and other heavy elements, (ii) enhanced amplitude of the coherent scattering by multiple electrons in atoms heavier than hydrogen and (iii) the contribution of the iron 6.4 keV line to the flux in the 4–8 keV band. For the molecular complex studied here, the estimate of the light front propagation velocity $v_z \sim 0.7c$ (C17a) implies the cosine of the scattering angle $\mu \sim -0.4$. For such a scattering angle the cross-section is slightly lower due to the angular dependence of Compton scattering $\propto (1 + \mu^2)$ and the values of $\eta(N_H)$ are close to the case of $\mu = 0$ (see Fig. 3). Below we assume $\sigma_{4-8} \approx 1.4\sigma_T$ to relate the X-ray surface brightness, the gas density and the luminosity of the primary source. The surface brightness of the same region measured by *Chandra* during 2015 observations is $I_X \sim 4.3 \times 10^{-13} \text{ erg s}^{-1} \text{ cm}^{-2} \text{ arcmin}^{-2}$ in the 4–8 keV band. Assuming $v_z = 0.7c$ the total energy emitted by Sgr A* during the flare is:

$$L_X \Delta t \sim \left(\frac{\bar{\rho}_H}{10^4 \text{ cm}^{-3}} \right)^{-1} \begin{cases} 3 \cdot 10^{46} \text{ erg}; & 4\text{--}8 \text{ keV} \\ 6 \cdot 10^{46} \text{ erg}; & 2\text{--}10 \text{ keV} \\ 2 \cdot 10^{47} \text{ erg}; & 1\text{--}100 \text{ keV}, \end{cases} \quad (8)$$

where conversion from 4–8 keV to other bands is done assuming photon index $\Gamma = 2$. This is consistent with our previous estimates (C17a), but now better justified value of mean density $\bar{\rho}_H \sim 10^4 \text{ cm}^{-3}$ is used instead of $\bar{\rho}_H \sim 10^3 \text{ cm}^{-3}$. Note that above estimate ignores the absorption and scattering due to molecular gas on the photon path from the primary source to the illuminated layer and then to the observer. Typical absorbing column density in the Galactic Center region is few 10^{22} cm^{-2} , which has a small impact on the 4–8 keV flux. However, the column density of the molecular cloud itself is $\sim \bar{\rho}_H \times 10 \text{ pc} \sim 3 \cdot 10^{23} \text{ cm}^{-2}$. Such column density would reduce the observed 4–8 keV flux by a factor of ~ 2 , increasing the estimate of the emitted power in equation (8) accordingly.

We can now combine equation (8) with the lower limit $L_{X,\min}$ on the Sgr A* luminosity (see Section 2.3.1) to obtain an upper limit on the duration of the flare:

$$\Delta t_{\max} \sim \frac{L_X \Delta t}{L_{X,\min}} \sim 1.6 \text{ yr}. \quad (9)$$

This value is consistent with constraints obtained so far from the light curves of individual clouds (e.g. Clavel et al. 2013). Shorter flares cannot be excluded, unless one increases the estimate of $L_{X,\min}$ (see Section 2.3.1) or finds very compact cloud with the light crossing time much shorter than a year (see Section 2.2.1). For instance, for the Eddington-level luminosity of $\sim 10^{44} \text{ erg s}^{-1}$, the duration of the flare can be as short as 1 h, setting aside a question of what mechanism is responsible for such short flare.

3 TOMOGRAPHY OF MOLECULAR CLOUDS

As discussed above, the apparent light curve of reflected emission in any given direction is a convolution of the intrinsic Sgr A* light curve with the gas density distribution along the line of sight. As a result, the observed light curve may (a) appear longer than the flare itself and (b) possess a complicated substructure even if the intrinsic flare lacks it. Moreover, in Section 2.3.2 we argue that the flare can be shorter than 1.6 yr (see equation 9), although this conclusion depends on the assumed mean density of the gas. Throughout the rest of the paper we consider the case of a short flare.

3.1 Probability distribution function of gas density

If the estimate of the duration $\Delta t \sim 1.6$ yr is approximately correct, than the physical size of the illuminated region along the line of sight is $\Delta z \sim 0.7c \Delta t \sim 0.2 \text{ pc} \times \frac{\Delta t}{1 \text{ yr}}$. At the same time, the arcsecond angular resolution of *Chandra* corresponds to scales $\Delta x \sim 0.04 \text{ pc}$.³ Thus, X-ray observations give us a view of a narrow ($<0.2 \text{ pc}$) density slice of the molecular cloud. Such data provide a direct probe of the density distribution that is not contaminated by projection effects. In particular, it should be possible to reconstruct the PDF(ρ). Indeed, according to equation (5) the surface brightness is proportional to the gas density, with the coefficient of proportionality set by the luminosity of the illuminating source, duration of the flare and geometrical factors. We note here that apart from the possible impact of the finite opacity, the relation between the density and the surface brightness is not sensitive to the physical state of the gas, i.e. the total mass density can be measured.

Numerical simulations and analytic arguments suggest that supersonic turbulence in the isothermal gas results in a log-normal PDF(ρ) (Vazquez-Semadeni 1994; Padoan, Nordlund & Jones 1997; Stone, Ostriker & Gammie 1998; Mac Low 1999; Ostriker, Stone & Gammie 2001; Kritsuk et al. 2007) with the characteristic width being determined by the Mach number of turbulent motions (Padoan, Nordlund & Jones 1997; Passot & Vázquez-Semadeni 1998; Kowal, Lazarian & Beresnyak 2007; Federrath, Klessen & Schmidt 2008; Molina et al. 2012). The corresponding density variance-Mach number scaling is in turn sensitive to whether the turbulence is mainly compressively (e.g. via accretion or shocks) or solenoidally (e.g. via externally induced shear) driven (Federrath, Klessen & Schmidt 2008), and also on whether the gas is isothermal or not (Nolan, Federrath & Sutherland 2015). As the

³ Of course, for off-axis angles larger than few arcminutes, the angular resolution of *Chandra* degrades significantly.

cloud evolves, the self-gravity leads to the formation of power-law tails in the high-density part of the density distribution (e.g. Ostriker, Gammie & Stone 1999; Klessen 2000; Federrath, Klessen & Schmidt 2008; Cho & Kim 2011; Kritsuk, Norman & Wagner 2011; Federrath & Klessen 2013; Girichidis et al. 2014; Burkhardt, Stalpes & Collins 2017).

This high-density tail is a key ingredient for determining the star formation rate and the star formation efficiency (e.g. Krumholz & McKee 2005; Elmegreen 2008; Hennebelle & Chabrier 2011; Padoan & Nordlund 2011; Salim, Federrath & Kewley 2015). Molecular clouds in the CMZ are of particular interest in this context, since they evolve in a very specific environment of the Galactic Center, and also because their measured star formation efficiency appears to be an order of magnitude lower compared to the molecular clouds in the Galactic disc (Longmore et al. 2013; Kruijssen et al. 2014; Ginsburg et al. 2016; Kauffmann et al. 2017a; Barnes et al. 2017). Measuring the PDF(ρ) over a broad range of the scales is a key for clarifying the particular mechanism(s) responsible for the suppression, e.g. high level of solenoidally forced turbulence (Federrath et al. 2016), and also whether this is a generic property of such an environment or it differs from a cloud to cloud, e.g. as a result of the different orbital evolution histories (Kauffmann et al. 2017b).

Thus, by measuring PDF(ρ) one gets insights on the driving mechanisms and the efficiency of star formation in a cloud. While the direct measurements of the PDF(ρ) from molecular emission lines is hindered by the projection effects, there is a hope that due to thinness of the illuminated slice X-ray data could be free from this limitation. Another potential advantage of X-rays is their high-penetrating power and insensitivity of the reflection efficiency to the physical state of the gas, unlike commonly used gas tracers that are sensitive to a certain range of densities determined by self-absorption and collisional de-excitation (e.g. Genzel 1991).

3.1.1 Illustrative simulation of an inhomogeneous gas distribution

To illustrate the possibility to recover the PDF(ρ), we simulated the illumination of a volume filled with inhomogeneous molecular gas. To this end, we used a simplified version of the recipe from Walch et al. (2011) to generate a $16 \times 16 \times 16$ pc cube with 0.0625 pc pixels. Namely, we first assign unit density to the whole cube. We then divide the cube into eight cub-subes, randomly select a fraction $f = 0.5$ of these sub-cubes and increase the density in the selected sub-cubes by a factor $C = 3.25$. The same procedure is iteratively repeated for each sub-cube with increased density until we reach the resolution of the cube. In addition, the density in the cube is modulated multiplicatively by an additional random field to slightly smooth the distribution. The resulting density field has a power-law spectrum with the slope that depends on f and C . Finally, the density is multiplied by a constant to obtain desired mean density $\langle \rho \rangle$ in the cube.

The cube centre is placed 20 pc away from the primary source in the sky plane and ~ 7 pc behind the source along the line of sight, approximately reproducing the position of molecular complex ('Bridge' and G0.11-0.11) studied in C17a. The illuminating source has a power-law spectrum with photon index $\Gamma = 2$. A small grid of models was run with the duration of the flare Δt varying between 0.6 and 9 yr. The luminosity of the flare L_X was adjusted to keep the total energy $L_X \Delta t$ constant (see Section 2.3.2). The reflected flux was calculated using a single scattering approximation, which is well suited for predicting the strength of the reflected emission (C17b).

Examples of the PDF(ρ) and PDF(I_X) obtained in the simulations are shown in Fig. 4 for $\langle \rho \rangle$ equal to 10^2 and 10^4 cm^{-3} (here the density ρ is the number density of hydrogen). In both plots the thick black line shows the PDF(ρ) (ρ is shown in the upper horizontal axis). The histograms in the same figure correspond to the predicted PDF(I_X) for flares with different durations (I_X is shown in the lower horizontal axis). The upper and lower horizontal axes are aligned such that in the optically thin limit, a given value of ρ corresponds to the value of I_X given by equations (5) and (7). For $\langle \rho \rangle = 10^2 \text{ cm}^{-3}$, the cloud is optically thin and for a short flare ($\Delta t = 0.6$ yr) the black histogram PDF(I_X) is an excellent proxy to the true underlying PDF(ρ).

3.1.2 Impact of the flare duration and spatial binning

As the duration of the flare increases, the size of the illuminated region along the line of sight Δz becomes larger than the size of dense clumps. As a result, I_X drops below the predictions for the case when the density is constant over entire illuminated region and the derived values of the surface brightness for the small and dense clumps moves to the left, forming a 'bump' in PDF(I_X). The amplitude of the bump increases as one moves to longer flares (see e.g. blue histogram in Fig. 4). The magnitude of this effect depends on how much mass is associated with small clumps. Indeed, in the optically thin limit the scattered flux is proportional to the total illuminated mass. Thus, the flux reflected by small clumps is conserved, but it is smeared over by averaging and contributes to lower surface brightness bins. In the simulations shown in Fig. 4, more mass is sitting on small scales, since $f \times C > 1$, and this makes the bump very prominent.

Qualitatively similar effect will be caused by averaging observations separated by a time longer than the light crossing time of dense clumps along the line of sight, since in individual observations each clump will be present only in some observations.

Similar 'migration' of I_X towards lower fluxes can be caused by limited spatial resolution, e.g. by binning the pixels in the image to achieve higher signal-to-noise ratio. This is illustrated by the green histogram in Fig. 4, which shows the effect of binning the image to 0.2 pc pixels (from the original resolution of ~ 0.06 pc).

3.1.3 Impact of the finite optical depth

Somewhat different results are obtained for the same setup, but with higher mean density $\langle \rho \rangle = 10^4 \text{ cm}^{-3}$ (see the right-hand panel of Fig. 4). In the simulated box, the column density increases at small scales (at each level of hierarchy the column density increases by a factor $C/2 \approx 1.6$). As a result, small clumps become optically thick, their reflection efficiency per unit mass decreases, and in the distribution of I_X they move to the left. Thus, a cut-off of the PDF(I_X) compared to underlying PDF(ρ) at large densities is the result of the opacity effects. The part of the PDF(I_X), corresponding to smaller densities, is recovered well. Unlike the optically thin case, the reflected flux associated with dense clumps is not conserved and the bump is much less pronounced. In addition, if the median value of the optical depth over entire region becomes significant, the attenuation for any line of sight contributes to an overall shift of the histogram towards lower fluxes (see right-hand panel of Fig. 4).

Qualitatively similar results were obtained by simulating a log-normal density distribution instead of a power law. This was done by generating many randomly positioned 3D structures (e.g. spheres) in a simulated volume. The sum of all structures overlapping at a

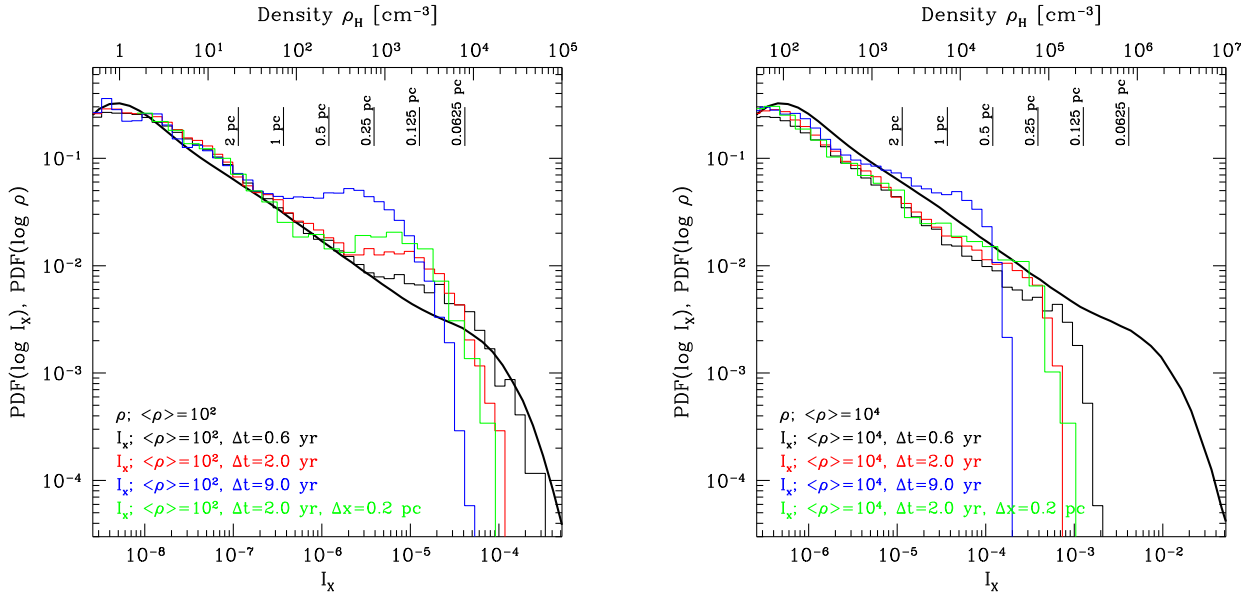


Figure 4. Simulated $\text{PDF}(\rho)$ and $\text{PDF}(I_X)$ for a molecular cloud illuminated by an X-ray flare from Sgr A*. The left- and right-hand panels correspond to the clouds with mean hydrogen densities 10^2 and 10^4 cm^{-3} , respectively. In both plots the thick black line shows the $\text{PDF}(\rho)$ (ρ is shown in the upper horizontal axis), while the histograms correspond to the observed $\text{PDF}(I_X)$ for flares with different durations (I_X is shown in the lower horizontal axis). The two horizontal axes are aligned such that in the optically thin limit a given value of ρ corresponds to the value of I_X , so that $\text{PDF}(\rho)$ and $\text{PDF}(I_X)$ can be compared directly. The cloud in the left-hand panel is optically thin and for a short flare ($\Delta t = 0.6 \text{ yr}$ the black ‘observed’ histogram reproduces well $\text{PDF}(\rho)$). As the duration of the flare increases, the size of the illuminated region along the line of sight Δz becomes larger than the size of small and dense cores and the value I_X moves to the left, forming a distinct bump in the $\text{PDF}(I_X)$ (see the text for details). For the denser cloud (right-hand panel), small clumps become optically thick and a cut-off in $\text{PDF}(I_X)$ develops towards high-density end. These simulations show that it is possible to recover $\text{PDF}(\rho)$ for the low-density part of the distribution, provided that the duration of the flare is sufficiently small.

given position gives $\log \rho$. The mean and the width of the resulting distribution can be controlled by choosing the volume filling factor and the value assigned to each structure. Thus generated density cube was used for simulations of the reflected emission (see Section 3.1.1). As before, in the optically thin case the density distribution is recovered well from the distribution of I_X . For the case, when the opacity is significant, both effects – (i) disappearance of the high column density clumps and (ii) overall shift of the PDF to the left due to distributed absorption – are present. The magnitudes of these effects depend on the distribution of the mass across spatial scales. When significant fraction of the mass is confined to a small number of very dense clumps, only those clumps are affected by the opacity, while the rest of $\text{PDF}(\rho)$ is preserved.

Of course, such simulations are not intended to reproduce realistic density PDF of molecular clouds. They show instead that (i) it is possible to recover $\text{PDF}(\rho)$ for the low-density part of the distribution, which is not affected by the opacity and (ii) the short flare case is a more direct tracer of the density distribution than the case when the duration of the flare is longer than few years.

3.1.4 $\text{PDF}(I_X)$ in the existing *Chandra* data and possible improvements

Shown in Fig. 5 is the observed $\text{PDF}(I_X)$, based on *Chandra* data taken in 2015 (see the right-hand panel in Fig. 1). To increase statistical significance of the measured reflection component flux in individual pixels, the image was binned to 4×4 arcsec pixels. The dotted vertical line shows the mean surface brightness over the region studied. The dashed line shows the log-normal distribution with $\sigma_s \approx 0.7$, where σ_s is the standard deviation of $\log I_X$. The standard deviation σ_I of the surface brightness normalized by the mean

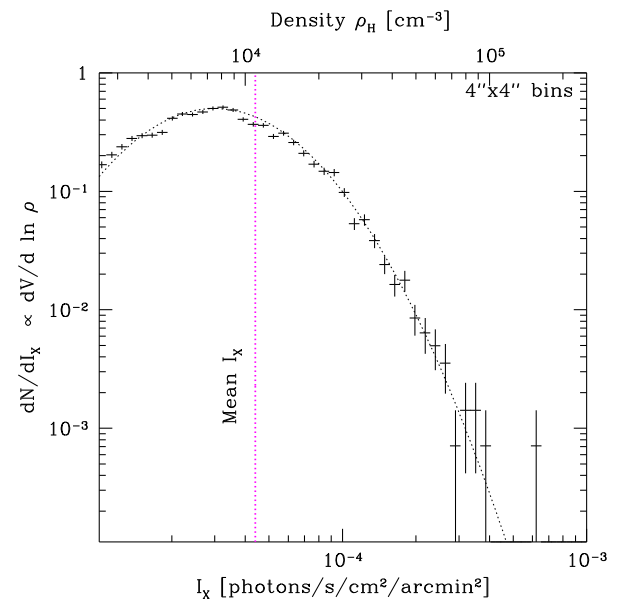


Figure 5. Observed Probability Distribution Function of the X-ray surface brightness I_X in the reflected component for 4 arcsec bins, corresponding to $\sim 0.16 \text{ pc}$. In the optically thin limit $\text{PDF}(I_X)$ is essentially $\text{PDF}(\rho)$ with proper transformation of arguments. The upper horizontal axis shows the density obtained by converting I_X to the gas density, using equation (5) in the limit of an optically thin cloud. The decline at large densities is either due to averaging over the bin’s volume, opacity effects or the paucity of small and dense clumps. The $\text{PDF}(I_X)$ based on the existing data is strongly affected by the photon counting noise, especially at low flux levels.

value can be obtained from σ_s as $\sigma_I = [\exp(\sigma_s^2) - 1]^{1/2} \sim 0.8$ (Price, Federrath & Brunt 2011). The upper horizontal axis shows the density, corresponding to a given I_X in the lower horizontal axis, assuming an optical thin case and using the value $L_X \Delta t$ estimated in Section 2.3.2. Therefore, the conversion to gas density bears the same level of uncertainties as $L_X \Delta t$.

While it is tempting to conclude that the density distribution is log-normal, two caveats have to be considered. First, the low flux part of the distribution (below $\sim 10^{-4}$ $\text{phots}^{-1} \text{cm}^{-2} \text{arcmin}^{-2}$) is strongly dominated by the statistical noise. Secondly, while the statistical uncertainty in getting I_X at high fluxes is not an issue, the measured distribution can suffer from the effects considered above, namely: opacity and time/space averaging, that could lead to a suppression of the high flux end of the distribution.

Some of these shortcomings can be eliminated in near future. For example, ongoing *Chandra* observations (PI: Maica Clavel) of the molecular clouds in the Galactic Center region should be able to constrain Δt sufficiently well to remove the uncertainty in the duration of the flare. These observations consist of several ~ 100 ks exposures spread over few years. Further progress is possible with an additional very deep (~ 1 Ms long) and continuous (to avoid smearing of image due to light propagation) *Chandra* observation. Such observation could help in several ways: (i) by improving the significance of flux measurements in the low surface brightness regions and therefore extending the dynamic range of the PDF(I_X) on the left side, (ii) by allowing for finer pixels and potentially extending the dynamic range on the high flux side and (iii) by making detailed spectral analysis of many small regions to better separate different components and estimating the optical depth for multiple bright regions. This, in particular, means that the accuracy of measuring the reflection emission intensity using the two-component decomposition method (see Section 2) can be thoroughly verified on the smallest scales. Although the narrow band map (close to 6.4 keV) does show a very similar morphology and a qualitatively similar PDF, the statistics in the narrow-band image is lower and the direct spectral analysis based on the longer exposure would be very helpful. Fig. 7 shows parameters of individual (isolated) clouds needed to provide at least 100 counts in the 4–8 keV band during 100 ks and 1 Ms observations. Going from 100 ks to 1 Ms exposure means that the densest clouds can be detected if their radii exceed ~ 1 arcsec approximately matching the *Chandra* angular resolution. For the low-density clouds, the size of the cloud corresponding to 100 counts may exceed the size of the illuminated region Δz along the line of sight. For such clouds, in Fig. 7 we make a correction to the expected flux, since only a fraction of the clouds volume is illuminated. Deep and almost continuous observations are crucial to improve the knowledge of the bright end of the PDF, corresponding to dense compact cores, since there the variability time-scales are expected to be very short. On the other hand, if the faint end of the PDF is due to the lower density and extended structure, the accumulation of the exposure over several years might still be helpful.

In addition, the results of more realistic numerical simulations of molecular clouds could be used to perform the analysis similar to that shown in Fig. 4. To this end we note that zoom-in numerical simulations have already reached the resolution of ~ 0.06 pc (Seifried et al. 2017), which is fully sufficient for confronting the models with the data of the current generation of X-ray observatories.

While the caveats discussed above can affect the derived PDF(ρ), it is interesting to speculate on the cloud characteristics, taking measured width of the log-normal distribution $\sigma_I \sim 0.8$ at the face value. Recently, Federrath et al. (2016) analysed the properties of the ‘Brick’ cloud, deriving $\sigma_{\rho/\rho_0} \sim 1.3$, and concluded that the width of

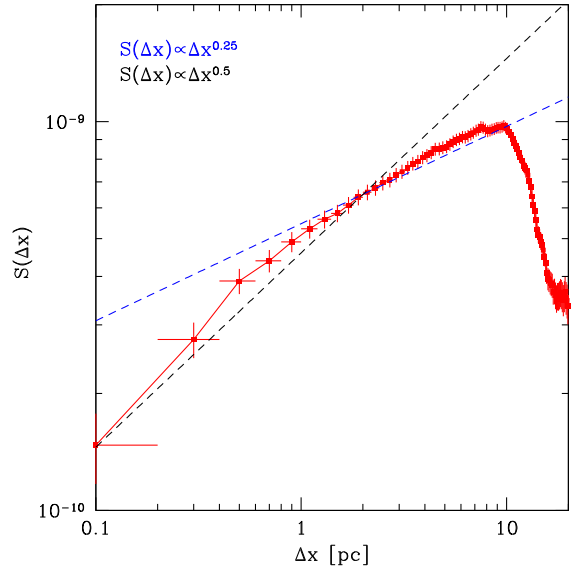


Figure 6. Second-order structure function $S(\Delta x)$ of the reflected emission obtained from *Chandra* observations in 2015. The same 4 arcsec binned image as in Fig. 5 is used. For comparison, two dashed lines show the power laws ($S \propto \Delta x^\eta$), with $\eta = 0.25$ and 0.5 . In simulations (see Federrath, Klessen & Schmidt 2009), such power laws (approximately) correspond to solenoidal and compressive drivings, respectively. The observed structure function of the reflected emission intensity may be affected by the duration of the flare (mostly on small scales), by the opacity effects and by the sampling variance and the choice of analysed region at larger scales. In particular, the drop of the structure function at largest Δx is clearly caused by the fact that the entire cloud is encompassed by the analysed region and the surface brightness is small on the opposite sides of the region.

the density PDF suggests a predominantly solenoidal driving of the turbulence in the cloud. Since the solenoidal driving is less efficient in promoting formation of dense cores, this result might explain a low star formation efficiency in the ‘Brick’ cloud as found by Kauffmann et al. (2017a,b). Assuming that in the cloud currently illuminated by the Sgr A* flare all conditions, except for the width of the PDF, are similar to those in the ‘Brick’, our value of σ_I will lead to even smaller values of turbulence driving parameter b (see Federrath et al. 2016, for the definition of this parameter). While it is clear that existing data are not yet sufficient to make a firm conclusion, the possibility of direct measurements of the density PDF for illuminated clouds looks very attractive.

3.2 Structure function of gas density

Another important characteristic of the molecular gas density distribution is the structure function. The second-order structure function of the density field is defined as

$$S(\Delta \mathbf{x}) = \langle [\rho(\mathbf{x}) - \rho(\mathbf{x} + \Delta \mathbf{x})]^2 \rangle, \quad (10)$$

where $\rho(\mathbf{x})$ is the density at a position \mathbf{x} . We assume that the structure function is isotropic, i.e. it depends on the absolute value of $\Delta \mathbf{x}$. In the optically thin limit (and a short flare), the structure function of the surface brightness can be used in lieu of the density field (see C17a). The structure function of the reflected emission obtained from *Chandra* images taken in 2015 is shown in Fig. 6. The same 4 arcsec binned image as in Fig. 5 was used to calculate the structure function. At small Δx it is shallower than the structure function

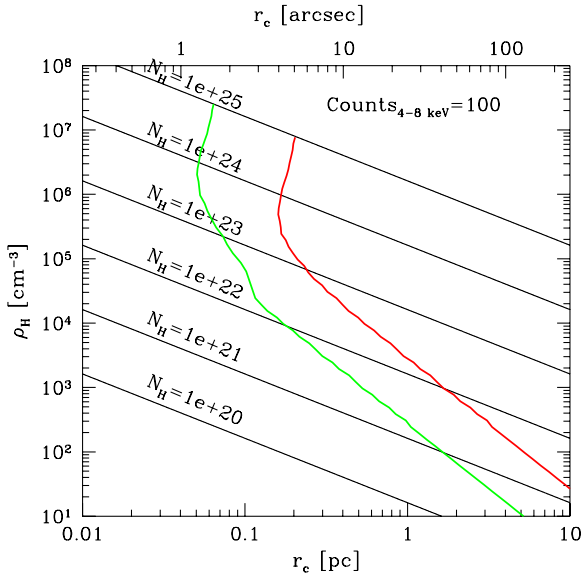


Figure 7. Prospects of detecting an isolated cloud in reflected emission with *Chandra* for different cloud sizes and densities during 100 ks (red curve) and 1 Ms (green curve) exposures, respectively. The size of the illuminated region along the line of sight is set to $\Delta z \approx 0.21$ pc. The sensitivity is defined by the requirement to get 100 counts in the 4–8 keV band to spectrally confirm the reflection nature of the emission. 1 Ms observation could help in several ways: (i) by improving the significance of flux measurements in the low surface brightness regions and therefore extending the dynamic range of the PDF(I_X) on the left-hand side (see Fig. 5), (ii) by allowing for finer pixels and potentially extending the dynamic range on the high flux side and (iii) by making detailed spectral analysis of many small regions to better separate different components and estimating the optical depth for multiple bright regions. Going from 100 ks to 1 Ms exposure means that the densest clouds can be detected if their radii exceed ~ 1 arcsec approximately matching *Chandra* angular resolution. Further increase of the exposure will not drastically improve the prospects of finding even smaller clouds, but might still be useful to map low surface brightness regions.

derived from the *XMM-Newton* data in C17a, due to the better angular resolution of *Chandra*. The slope of $S(\Delta x)$ can be used to place constraints on the internal structure of the molecular gas. For instance, two dashed lines show the power laws ($S \propto \Delta x^\eta$), with $\eta = 0.25$ and 0.5 . In the simulation of Federrath, Klessen & Schmidt (2009), such power laws (approximately) correspond to solenoidal and compressive drivings, respectively. As in Section 3.1.4, taking at the face value this comparison hints on larger role of the solenoidal driving. We reiterate here that the observed PDF and the structure function can suffer from the sampling variance, especially for large Δx . For instance, the drop of the structure function at largest Δx is clearly caused by the fact that the entire cloud is encompassed by the analysed region and the surface brightness is small on the opposite sides of the region. At small Δx , the structure function can be sensitive to the duration of the flare, angular resolution of the telescope and the opacity of dense clumps.

3.3 Gas velocities from high-resolution spectroscopy

In this section we briefly outline new diagnostics that is difficult to do now, but will become possible with future X-ray observatories.

High-energy resolution coupled with high angular resolution will become available with missions like *ATHENA* (Nandra et al. 2013) and *Lynx* (formerly X-Ray Surveyor; Vikhlinin et al. 2012). For the reflected emission this implies that using fluorescent lines,

one can measure line-of-sight velocities of the gas illuminated by Sgr A* with the accuracy of few km s^{-1} . Presumably, by that time, Δt , t_{age} and L_X [or more generally, entire $L_X(t)$] will already be reliably known (see Section 2.2 above). Thus, for any clump bright in the reflected emission we will know both the line-of-sight position z and the line-of-sight velocity v_z . Such data would dramatically broaden the possibility to use Sgr A* illumination as a diagnostic tool, as we briefly outline below.

(i) *Kinematics of molecular clouds.* Since the z coordinate is effectively measured with respect to the illuminating source – Sgr A*, i.e. the dynamic centre of the Galaxy, a pair of values (z , v_z) provides an important piece of information on the molecular gas kinematics. For instance, one can immediately verify if the clouds are on the low eccentricity orbits in the gravitational potential of the central part of the Milky Way. This test can be further enhanced by using variations of v_z with l and b .

Furthermore, suppose that some masers can be associated with selected dense clumps, illuminated by Sgr A*. Suppose further that peculiar motions of these masers in the sky plane can be measured. Then for these masers/clumps we will know both accurate 3D positions and all velocity components.

(ii) *Structure function of the gas velocity field.* On small scales one can hope to measure the structure function of the gas velocity field. From a single observation the information on the structure function in the direction perpendicular to v_z can be obtained. Multiple observations, spread over few years, would provide data on the v_z variations along the z direction. The degree of accuracy that can be achieved crucially depends on the spectral resolution of future observatories. We note here that detecting velocity broadening in unresolved clumps (rather than variations of the line centroid) may be very challenging for X-ray observatories.

(iii) *Combining X-ray and molecular line data.* Having $v_z(l, b, z)$ and $\rho(l, b, z)$, one can combine these data with position–position–velocity data on molecular lines to recover 3D distribution of molecular tracers. The accuracy of this procedure will depend on the amplitude of the velocity gradients and the spectral resolution of future missions. A by-product of the above procedure is a detailed piece of information of the molecular line fluxes from the gas with a given density, at least for clouds not affected by the absorption of either X-rays (say, 4–8 keV) or molecular lines. Of course, these data can also be used to make constraints on the excitation mechanisms of specific lines.

This is, of course, not an exhaustive list of possibilities, but just a few examples, illustrating the power of a combination of Sgr A* flares and molecular clouds.

4 CONCLUSIONS

Illumination of molecular clouds in the CMZ by a powerful X-ray flare of Sgr A* can be used to study the properties of such flare, even although it occurred more than a hundred years ago. The same flare can be used to probe the inner structure of molecular clouds. The better we know the properties of the flare, the better are the constraints on the properties of molecular gas, and vice versa. In Section 1 we outline a long-term road-map of improving our knowledge of both sides of the problem (see Table 1).

In Section 2 we summarize the approaches that can be used to constrain the properties of the flare. Some basic characteristics can already be measured from the existing data, albeit with low accuracy. For instance, the age of the outburst and the lower limit on the luminosity of Sgr A* during the flare can be estimated from

existing *XMM-Newton* and *Chandra* data. The estimate of the total energy emitted by Sgr A* during the flare depends on the assumption that the mean density of illuminated gas can be estimated from molecular tracers. Assuming that this estimate is correct, the duration of the flare turns out to be short, of the order of years. Further improvements in the accuracy of flare characterization is possible with additional X-ray observations, largely based on pure geometrical arguments and making more accurate evaluation of structure functions of reflected emission in time and space domains. Future X-ray polarimetric observations would also help to eliminate remaining uncertainties, in particular, testing the main assumption that the source of illuminating photons is indeed Sgr A*. The best chance to probe the full light-curve of the flare could come from observations of a compact and relatively isolated clouds (yet to be identified in the data). If such cloud is found and monitored over several years, then its light curve will be a direct proxy of the flare light curve. Knowing the light curve, one can use this information in order to more accurately reconstruct 3D distribution of the molecular gas.

If the flare was indeed very short, the illumination of molecular clouds in the CMZ opens a unique opportunity to do in-depth diagnostics of molecular gas. Particularly attractive is the possibility to avoid projection effects, since the layer of illuminated gas can be very thin (smaller than a parsec). We argue that deep X-ray observations with *Chandra* can provide direct measurements of the probability distribution function of the molecular gas density PDF(ρ) and the density structure function $S(\Delta x)$ on sub-pc scales, while future observatories like *ATHENA* or *Lynx* will be able to reconstruct the 3D velocity field of the molecular gas and to measure the velocity structure function.

The relation between the reflected flux and the gas density is straightforward, since the X-ray flux probes directly the gas density, being weakly sensitive to its ionization state, temperature or chemical composition. This approach has only three principal limitations: (i) duration of the flare, which sets the minimal scales that can be probed; (ii) opacity effects, which for photons above ~ 4 keV become severe for the hydrogen column densities above $\sim 3 \times 10^{23} \text{ cm}^{-2}$; and (iii) sampling variance. It is likely that the impact of the first two effects will become clear in the near future from the ongoing *Chandra* observations. The latter limitation is especially important on largest scales (few pc – 10 pc) and can only be eliminated by finding more illuminated clouds, which will allow more accurate determination of the Sgr A*'s flare parameters, as well as more tight constraints on the properties of molecular clouds.

While today the estimates of the flare age (see C17a) and other parameters are still very uncertain, potentially the analysis of reflected emission could become the most accurate source of information on the clouds positions relative to Sgr A*, their kinematics and small-scale substructure.

ACKNOWLEDGEMENTS

The results reported in this article are based in part on data obtained from the *Chandra* X-ray Observatory (NASA) Data Archive, OBSIDs: 17236 and 17239. We acknowledge partial support by grant No. 14-22-00271 from the Russian Scientific Foundation.

REFERENCES

Baganoff F. K. et al., 2003, *ApJ*, 591, 891
 Barnes A. T., Longmore S. N., Battersby C., Bally J., Kruijssen J. M. D., Henshaw J. D., Walker D. L., 2017, *MNRAS*, 469, 2263

Boldyrev S., 2002, *ApJ*, 569, 841
 Brunt C. M., Federrath C., Price D. J., 2010, *MNRAS*, 405, L56
 Burkhardt B., Stalpes K., Collins D. C., 2017, *ApJ*, 834, L1
 Capelli R., Warwick R. S., Porquet D., Gillessen S., Predehl P., 2012, *A&A*, 545, A35
 Cho W., Kim J., 2011, *MNRAS*, 410, L8
 Churazov E. et al., 1993, *A&AS*, 97, 173
 Churazov E., Sunyaev R., Sazonov S., 2002, *MNRAS*, 330, 817
 Churazov E., Khabibullin I., Sunyaev R., Ponti G., 2017a, *MNRAS*, 465, 45
 Churazov E., Khabibullin I., Ponti G., Sunyaev R., 2017b, *MNRAS*, 468, 165
 Clark P. C., Glover S. C. O., Klessen R. S., Bonnell I. A., 2012, *MNRAS*, 424, 2599
 Clavel M., Terrier R., Goldwurm A., Morris M. R., Ponti G., Soldi S., Trap G., 2013, *A&A*, 558, A32
 Clavel M., Soldi S., Terrier R., Goldwurm A., Morris M. R., Ponti G., 2014, *sf2a.conf*, 85
 Couderc P., 1939, *AnAp*, 2, 271
 Elmegreen B. G., 2008, *ApJ*, 672, 1006
 Elmegreen B. G., Scalo J., 2004, *ARA&A*, 42, 211
 Federrath C., Klessen R. S., 2013, *ApJ*, 763, 51
 Federrath C., Klessen R. S., Schmidt W., 2008, *ApJ*, 688, L79
 Federrath C., Klessen R. S., Schmidt W., 2009, *ApJ*, 692, 364
 Federrath C., Roman-Duval J., Klessen R. S., Schmidt W., Mac Low M.-M., 2010, *A&A*, 512, A81
 Federrath C. et al., 2016, *ApJ*, 832, 143
 Genzel R., 1991, *ASIC*, 342, 155
 Ginsburg A. et al., 2016, *A&A*, 586, A50
 Girichidis P., Konstandin L., Whitworth A. P., Klessen R. S., 2014, *ApJ*, 781, 91
 Guillochon J., Loeb A., MacLeod M., Ramirez-Ruiz E., 2014, *ApJ*, 786, L12
 Hennebelle P., Chabrier G., 2011, *ApJ*, 743, L29
 Kainulainen J., Federrath C., Henning T., 2014, *Sci*, 344, 183
 Kauffmann J., Pillai T., Zhang Q., Menten K. M., Goldsmith P. F., Lu X., Guzmán A. E., 2017a, *A&A*, 603, A89
 Kauffmann J., Pillai T., Zhang Q., Menten K. M., Goldsmith P. F., Lu X., Guzmán A. E., Schmiedeke A., 2017b, *A&A*, 603, A90
 Klessen R. S., 2000, *ApJ*, 535, 869
 Klessen R. S., Glover S. C. O., 2016, *SAAS*, 43, 85
 Kowal G., Lazarian A., Beresnyak A., 2007, *ApJ*, 658, 423
 Koyama K., Maeda Y., Sonobe T., Takeshima T., Tanaka Y., Yamauchi S., 1996, *PASJ*, 48, 249
 Kritsuk A. G., Norman M. L., Padoan P., Wagner R., 2007, *ApJ*, 665, 416
 Kritsuk A. G., Norman M. L., Wagner R., 2011, *ApJ*, 727, L20
 Krivonoz R. et al., 2017, *MNRAS*, 468, 2822
 Kruijssen J. M. D., Longmore S. N., Elmegreen B. G., Murray N., Bally J., Testi L., Kennicutt R. C., 2014, *MNRAS*, 440, 3370
 Krumholz M. R., McKee C. F., 2005, *ApJ*, 630, 250
 Longmore S. N. et al., 2013, *MNRAS*, 429, 987
 Mac Low M.-M., 1999, *ApJ*, 524, 169
 Mac Low M.-M., Klessen R. S., 2004, *RvMP*, 76, 125
 Marin F., Muleri F., Soffitta P., Karas V., Kunneriath D., 2015, *A&A*, 576, A19
 McKee C. F., Ostriker E. C., 2007, *ARA&A*, 45, 565
 Mills E. A. C., Battersby C., 2017, *ApJ*, 835, 76
 Molaro M., Khatri R., Sunyaev R. A., 2016, *A&A*, 589, A88
 Molina F. Z., Glover S. C. O., Federrath C., Klessen R. S., 2012, *MNRAS*, 423, 2680
 Mori K. et al., 2015, *ApJ*, 814, 94
 Muno M. P., Baganoff F. K., Brandt W. N., Park S., Morris M. R., 2007, *ApJ*, 656, L69
 Nandra K. et al., 2013, preprint ([arXiv:1306.2307](https://arxiv.org/abs/1306.2307))
 Nolan C. A., Federrath C., Sutherland R. S., 2015, *MNRAS*, 451, 1380
 Ostriker E. C., Gammie C. F., Stone J. M., 1999, *ApJ*, 513, 259
 Ostriker E. C., Stone J. M., Gammie C. F., 2001, *ApJ*, 546, 980
 Padoan P., Nordlund Å., 2002, *ApJ*, 576, 870
 Padoan P., Nordlund Å., 2011, *ApJ*, 730, 40

- Padoan P., Nordlund A., Jones B. J. T., 1997, *MNRAS*, 288, 145
 Passot T., Vázquez-Semadeni E., 1998, *PhRvE*, 58, 4501
 Ponti G., Terrier R., Goldwurm A., Belanger G., Trap G., 2010, *ApJ*, 714, 732
 Ponti G., Morris M. R., Terrier R., Goldwurm A., 2013, *ASSP*, 34, 331
 Price D. J., Federrath C., Brunt C. M., 2011, *ApJ*, 727, L21
 Ryu S. G., Nobukawa M., Nakashima S., Tsuru T. G., Koyama K., Uchiyama H., 2013, *PASJ*, 65, 33
 Salim D. M., Federrath C., Kewley L. J., 2015, *ApJ*, 806, L36
 Seifried D. et al., 2017, preprint ([arXiv:1704.06487](https://arxiv.org/abs/1704.06487))
 Soffitta P. et al., 2013, *ExA*, 36, 523
 Stone J. M., Ostriker E. C., Gammie C. F., 1998, *ApJ*, 508, L99
 Stutzki J., Bensch F., Heithausen A., Ossenkopf V., Zielinsky M., 1998, *A&A*, 336, 697
 Sunyaev R. A., Churazov E. M., 1996, *AstL*, 22, 648
 Sunyaev R., Churazov E., 1998, *MNRAS*, 297, 1279
 Sunyaev R. et al., 1991, *ApJ*, 383, L49
 Sunyaev R. A., Markevitch M., Pavlinsky M., 1993, *ApJ*, 407, 606
 Sunyaev R. A., Uskov D. B., Churazov E. M., 1999, *AstL*, 25, 199
 Terrier R. et al., 2010, *ApJ*, 719, 143
 Vainshtein L. A., Syunyaev R. A., Churazov E. M., 1998, *AstL*, 24, 271
 Vazquez-Semadeni E., 1994, *ApJ*, 423, 681
 Vikhlinin A. et al., 2012, *SPIE*, 8443, 844316
 Walch S., Whitworth A., Bisbas T., Wünsch R., Hubber D., 2011, *IAUS*, 270, 323
 Walch S. K., Whitworth A. P., Bisbas T., Wünsch R., Hubber D., 2012, *MNRAS*, 427, 625
 Walls M., Chernyakova M., Terrier R., Goldwurm A., 2016, *MNRAS*, 463, 2893
 Weisskopf M. C. et al., 2013, *SPIE*, 8859, 885908
 Zhang S. et al., 2015, *ApJ*, 815, 132
 Zubovas K., Nayakshin S., Markoff S., 2012, *MNRAS*, 421, 1315

This paper has been typeset from a \TeX/L\TeX file prepared by the author.